

Spontaneous helical order of a chiral p-wave superfluid confined in nano-scale channels

J. J. Wiman and J. A. Sauls*

Department of Physics and Astronomy, Northwestern University, Evanston, IL 60208

(Dated: August 14, 2018)

Strong interactions that favor chiral p-wave pairing, combined with strong pair breaking by confining boundaries, are shown to lead to new equilibrium states with different broken symmetries. Based on a strong-coupling extension of the Ginzburg-Landau (GL) theory that accurately accounts for the thermodynamics and phase diagram of the bulk phases of superfluid ^3He , we predict new phases of superfluid ^3He for confined geometries that spontaneously break rotational and translational symmetry in combination with parity and time-reversal symmetry. One of the newly predicted phases exhibits a unique combination of chiral and helical order that is energetically stable in cylindrical channels of radius approaching the Cooper pair coherence length, e.g. $R \sim 100\text{nm}$. Precise numerical minimization of the free energy yields a broad region of stability of the helical phase as a function of pressure and temperature, in addition to three translationally invariant phases with distinct broken spin- and orbital rotation symmetries. The helical phase is stable at both high and low pressures and favored by boundaries with strong pair-breaking. We present calculations of transverse NMR frequency shifts as functions of rf pulse tipping angle, magnetic field orientation, and temperature as signatures of these broken symmetry phases.

Introduction — The superfluid phases of ^3He are paradigms for spontaneous symmetry breaking in condensed matter and quantum field theory [1, 2]. The bulk A- and B phases are BCS condensates of p-wave, spin-triplet Cooper pairs [3]. The broken symmetries of these phases, which are well established, underpin the non-trivial topologies of both ground states [4, 5]. However, the bulk phases are only *two realizations* of the 18-dimensional manifold of spin-triplet, p-wave condensates. When ^3He is subjected to a confining potential on scales approaching the Cooper pair coherence length, $\xi_0 \approx 160 - 770 \text{Å}$ depending on pressure, new ground states with novel broken symmetries are stabilized [6–9].

In this Letter we report theoretical predictions of the equilibrium phases of superfluid ^3He when confined in quasi-one-dimensional channels with radial confinement ranging from $R = 2 - 20 \xi_0(p)$. Among these phases is a novel “helical” phase of ^3He that spontaneously breaks both time-reversal and translational symmetry along the channel. The broken translational symmetry is realized as a *double helix* of disclination lines of the chiral axis confined on the boundary of the cylinder walls. The double-helix phase is predicted to be stable over a large region of the pressure-temperature phase diagram for channels with radius $R = 100\text{nm}$.

Ginzburg-Landau Theory — Our results are based on a strong-coupling extension of Ginzburg-Landau (GL) theory that accurately reproduces the relative stability of the bulk A- and B-phases, including the A-B phase transition [8]. The GL theory is formulated as a functional of the order parameter, the condensate amplitude for Cooper pairs, $\langle \psi_\sigma(\mathbf{p}) \psi_{\sigma'}(-\mathbf{p}) \rangle$ in the spin-momentum basis. For spin-triplet, p-wave Cooper pairs the order parameter can be expressed in terms of a 3×3 matrix $A_{\alpha i}$ of complex amplitudes that transforms as the vector representation of $\text{SO}(3)_S$ with respect to the spin index α , and as the vector representation of $\text{SO}(3)_L$ with respect to the orbital momentum index i . In cylindrical coordinates the order pa-

rameter matrix may be represented as

$$A = \begin{pmatrix} A_{rr} & A_{r\phi} & A_{rz} \\ A_{\phi r} & A_{\phi\phi} & A_{\phi z} \\ A_{zr} & A_{z\phi} & A_{zz} \end{pmatrix}, \quad (1)$$

where we choose aligned spin and orbital coordinate axes. The GL free energy functional,

$$\Omega[A] = \int_V d^3r (f_{\text{bulk}}[A] + f_{\text{grad}}[A]), \quad (2)$$

is expressed in terms of a bulk free energy density [10],

$$\begin{aligned} f_{\text{bulk}}[A] = & \alpha(T) \text{Tr}(AA^\dagger) + \beta_1 |\text{Tr}(AA^T)|^2 \\ & + \beta_2 [\text{Tr}(AA^\dagger)]^2 + \beta_3 \text{Tr}[AA^T(AA^T)^*] \\ & + \beta_4 \text{Tr}[(AA^\dagger)^2] + \beta_5 \text{Tr}[AA^\dagger(AA^\dagger)^*], \end{aligned} \quad (3)$$

and the gradient energies,

$$f_{\text{grad}}[A] = K_1 A_{\alpha j, k}^* A_{\alpha j, k} + K_2 A_{\alpha j, j}^* A_{\alpha k, k} + K_3 A_{\alpha j, k}^* A_{\alpha k, j}, \quad (4)$$

where A^\dagger (A^T) is the adjoint (transpose) of A , $A_{\alpha i, j} = \partial_j A_{\alpha i}$, and the transformation of the gradient free energy from the Cartesian representation to cylindrical coordinates given in Eq. (6) of Ref. 8. The material parameters, α , $\{\beta_i | i = 1 \dots 5\}$, and $\{K_a | a = 1, 2, 3\}$ multiplying the invariants defining the GL functional are determined by the microscopic pairing theory for ^3He . In weak-coupling theory these parameters are given in Refs. 8 and 10.

Ginzburg-Landau theory is widely used in studying inhomogeneous superconducting phases, notably vortex states in type II superconductors [11], as well as Fulde-Ferrell-Larkin-Ovchinnikov states at high field and low temperatures [12]. In the case of ^3He a strong-coupling extension of the weak-coupling GL theory that accounts for the relative stability of the bulk A- and B phases, and specifically the A-B transition line, $T_{AB}(p)$ for pressures above the polycritical point, $p \gtrsim p_c$ was introduced in Ref. 8. The strong-coupling functional is defined by the corrections to the fourth-order weak-coupling material parameters,

$$\beta_i(p, T) = \beta_i^{\text{wc}}(p, T_c(p)) + \frac{T}{T_c} \Delta \beta_i^{\text{sc}}(p), \quad (5)$$

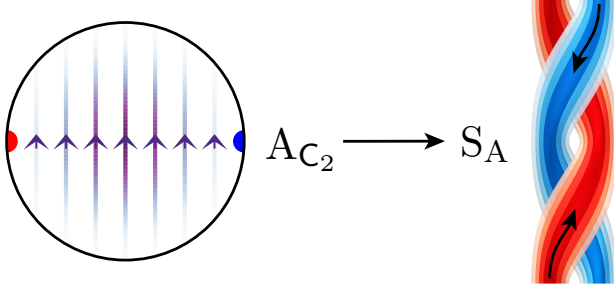


FIG. 1. Left: The chiral axis $\hat{l}(\mathbf{r})$ for the AC_2 phase at $p = 26$ bar, $T = 0.7 T_c$ with strong pairbreaking ($b'_T = 0.1$). The chiral axis is confined in the $r - \phi$ plane. The arrow color density is scaled by the amplitude, $(\Delta_r^2 + \Delta_\phi^2)^{1/2}$. The red and blue dots locate the two disgyrations, which support supercurrents propagating along $+z$ and $-z$, respectively. Right: Supercurrent isosurfaces in the SA phase, calculated using the full order parameter in Eq. 13 of the Appendix.

with $\Delta\beta_i^{\text{sc}}(p) = \beta_i(p, T_c(p)) - \beta_i^{\text{wc}}(p, T_c(p))$. The weak-coupling parameters, $\beta_i^{\text{wc}}(p, T_c(p))$ are calculated from a Luttinger-Ward formulation of the weak-coupling microscopic free-energy functional and evaluated using the known pressure-dependent Fermi-liquid material parameters, provided in Table I of Ref. 8. The $\Delta\beta_i^{\text{sc}}(p)$ have been obtained from analysis of measurements of the strong-coupling enhancement of heat capacity jumps, NMR frequency shifts and the Zeeman splitting of superfluid transition in a magnetic field [13]. The results we report are based on the strong-coupling parameters reported in Table I of Ref. [8]. We emphasize that the extended GL functional accounts for the relative stability of competing phases at temperatures well below $T_c(p)$, including the bulk A and B phases at high pressures [8], and the A to stripe phase transition in thin films of ^3He [9], and in the former case has been validated by our microscopic calculations of $T_{AB}(p)$ and the strong-coupling beta parameters, $\Delta\beta_i^{\text{sc}}(p)$, based on the formulation of the strong-coupling theory developed in Refs. 14–17.

The geometry we consider here is an infinitely long cylindrical channel of radius R . For the channel walls we use boundary conditions that include a variable order parameter “slip length” b_T inspired by the analysis of Ambegaokar, de Gennes, and Rainer [18], as well as the influence of boundary curvature [19]. The resulting conditions at $r = R$ are [8],

$$A_{\alpha r}|_{r=R} = 0, \quad \frac{\partial A_{\alpha z}}{\partial r}\bigg|_{r=R} = -\frac{1}{b_T} A_{\alpha z}|_{r=R},$$

$$\frac{\partial A_{\alpha\phi}}{\partial r}\bigg|_{r=R} = \left(\frac{1}{R} - \frac{1}{b_T}\right) A_{\alpha\phi}|_{r=R}. \quad (6)$$

where the transverse extrapolation parameter $b'_T \equiv b_T/\xi_0$ varies between the $b'_T \rightarrow 0$ (maximal pairbreaking) and $b'_T \rightarrow \infty$ (minimal pairbreaking) limits.

The equilibrium order parameter is obtained by minimizing the GL free energy functional, i.e. by solving the Euler-Lagrange equations, $\delta\Omega[A]/\delta A^\dagger = 0$. When restricted to translationally invariant states we obtain four

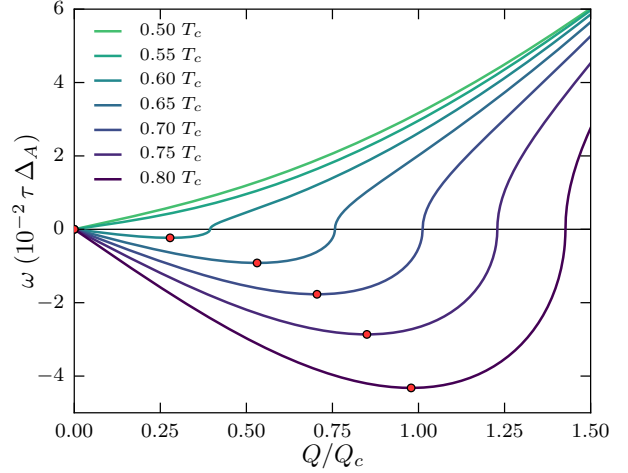


FIG. 2. NG mode dispersion, ω_- , as a function of Q and T and scaled by the bulk A-phase amplitude at $p = 26$ bar and $R = 100$ nm. Negative values denote imaginary values of ω_- . The circles indicate the most unstable mode, Q/Q_c , for each temperature. $Q_c \approx \pi/674 \text{ nm} = 4.66 \times 10^{-3} \text{ nm}^{-1}$ is the maximum value of the most unstable mode at the SA - P_z transition.

phases stable in different regions of the $p - T$ phase diagram: the P_z phase with Cooper pairs nematically aligned along the axis of the cylindrical channel is the first unstable mode from the normal state. At a lower temperature Cooper pairs with orbital wave functions transverse to z become unstable. Strong-coupling and strong pair breaking on the boundary lead to two distinct chiral phases with different symmetries. The first is a second-order transition from the P_z phase to the AC_2 phase with the chiral axis aligned in the plane perpendicular to the z axis. The AC_2 phase spontaneously breaks $SO(2)$ rotation symmetry. At lower temperatures the cylindrically isotropic chiral phase, $ASO(2)$, is stabilized, and at even lower temperatures, the polar-distorted $BSO(2)$ phase is favored. Both $ASO(2)$ and $BSO(2)$ phases are separated by first-order transitions [8].

Dynamical Instability — The chiral AC_2 phase is an inhomogeneous analog of bulk ^3He -A, with a spatially averaged angular momentum (chiral) axis $\langle \hat{l} \rangle$ aligned along a fixed but arbitrary direction in the $r - \phi$ plane, as shown in Figure 1. For maximal pairbreaking boundary conditions the AC_2 order parameter is given by

$$A_{\alpha i} = \hat{d}_\alpha \cos\left(\frac{\pi r}{2R}\right) \left\{ \Delta'_z \hat{z}_i + i \Delta''_r (\cos(\phi - \vartheta) \hat{r}_i - \sin(\phi - \vartheta) \hat{\phi}_i) \right\}. \quad (7)$$

where $\vartheta + \pi/2$ is the angle of the average direction of the angular momentum axis, $\langle \vec{l} \rangle$ in the $r - \phi$ plane. The in-plane chiral axis spontaneously breaks the continuous $SO(2)$ rotational symmetry of the confining potential. The corresponding continuous degeneracy of the AC_2 phase implies the existence of a Nambu-Goldstone (NG) mode associated with massless, long-wavelength excitation of the orientation, ϑ , of $\langle \vec{l} \rangle$.

The dynamical equation for the NG mode is obtained from the action for the space-time fluctuations of the

Cooper pairs relative to the A_{C_2} ground state, $\mathcal{A}_{\alpha i}(\mathbf{r}, t) = A_{\alpha i}(\mathbf{r}, t) - A_{\alpha i}^{A_{C_2}}(\mathbf{r})$,

$$S = \int_V dt d^3r \{ \tau \text{Tr}(\mathcal{A} \mathcal{A}^\dagger) - \mathcal{U}[\mathcal{A}] \}, \quad (8)$$

where $\mathcal{U}[\mathcal{A}]$ is the effective potential derived from an expansion of the free energy functional, $\Omega[A]$, to quadratic order in the fluctuations, \mathcal{A} , of order parameter. The additional invariant represents the kinetic energy of the Cooper pair fluctuations, with the effective inertia given by $\tau = 7\zeta(3)N_f/48(\pi k_B T_c)^2$ in the weak-coupling BCS limit [20], where N_f is the normal-state density of states at the Fermi energy.

For the NG mode the action is a functional of the degeneracy variable corresponding to space-time fluctuations of the orientation of the chiral axis, $\vartheta(t, z)$, and the fluctuations of the polar component of the Cooper amplitude, $\delta_z''(t, z)$, that couples linearly to $\vartheta(t, z)$ through the gradient energy. The order parameter that incorporates these fluctuations is

$$A_{\alpha i} = \hat{d}_\alpha \cos\left(\frac{\pi r}{2R}\right) \left\{ i \Delta_r'' \cos[\phi - \vartheta(t, z)] \hat{r}_i - i \Delta_r'' \sin[\phi - \vartheta(t, z)] \hat{\phi}_i + \Delta_z' \hat{z}_i \right\} - i \delta_z''(t, z) \sin\left(\frac{\pi r}{R}\right) \sin[\phi - \vartheta(t, z)] \hat{d}_\alpha \hat{z}_i, \quad (9)$$

where Δ_r'' and Δ_z' take their equilibrium values found by minimizing the free energy functional with the order parameter in Eq. 7. Since the fluctuations depend only on time, t , and the coordinate, z , along the channel, we can integrate out the dependences on r and ϕ . We then express the action in Fourier space, in which case we obtain a sum over independent Fourier modes of the form, $\vartheta(t, z) = \vartheta \cos(\omega t + Qz)$ and $\delta_z''(t, z) = \delta_z'' \sin(\omega t + Qz)$. The Euler-Lagrange equations reduce to eigenvalue equations for the coupled mode amplitudes,

$$\omega^2 \vartheta = c^2 Q^2 \vartheta + \frac{8(3\pi - 4)}{9(\pi^2 - 4)\Delta_r''} \left(\frac{\pi c}{R}\right) c Q \delta_z'' \quad (10)$$

$$\omega^2 \delta_z'' = \frac{1}{\tau} \left\{ \alpha + \left(1 - \frac{16}{9\pi^2}\right) (\beta_{13} + \beta_{245})(\Delta_r''^2 + \Delta_z'^2) + 3c^2 Q^2 + \left(\frac{\pi c}{R}\right)^2 \left[1 + \frac{2}{\pi^2} \text{Cin}(2\pi)\right] \right\} \delta_z'' + \frac{16(3\pi - 4)\Delta_r''}{9\pi^2} \left(\frac{\pi c}{R}\right) c Q \vartheta, \quad (11)$$

where $\text{Cin}(2\pi) = \int_0^{2\pi} du (1 - \cos u)/u$. The weak-coupling relation $K_1 = K_2 = K_3 \equiv K$ has been used, and we introduced the velocity, $c \equiv \sqrt{K/\tau} = v_f/\sqrt{5}$, where v_f is the Fermi velocity.

There are two eigenmodes corresponding to bosonic excitations with dispersions $\omega_\pm(Q)$. The low frequency mode, $\omega_-(Q)$ is identified as the NG mode with an excitation that is a pure rotation by ϑ , with a linear dispersion $\omega_-(Q) \propto Q$ for $Q \rightarrow 0$. Indeed the A_{C_2} phase supports low-frequency bosonic excitations corresponding to oscillations of the chiral axis, as shown in Fig. 2 for $R = 100$ nm,

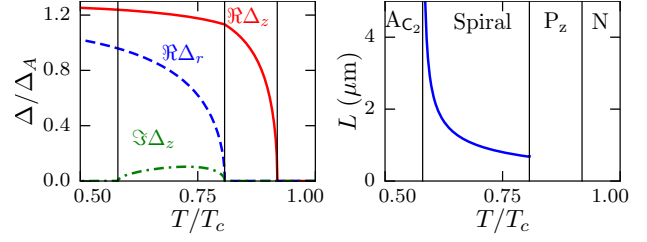


FIG. 3. (Left) The amplitudes Δ_z' (red); Δ_r'' (blue); and Δ_z'' (green) for the S_A order parameter phase, at $p = 26$ bar, $R = 100$ nm and scaled by the bulk A phase amplitude $\Delta_A = \sqrt{|\alpha(T)|/4\beta_{245}}$. The black vertical lines denote the continuous phase transitions A_{C_2} - S_A , S_A - P_z , and P_z -Normal with increasing temperature. (Right) The temperature dependence of the half-period L .

$p = 26$ bar and $T/T_c = 0.5$. However, the mode softens as the temperature increases. Above a critical temperature of $T^* \approx 0.57T_c$ the stiffness supporting the NG mode vanishes, and a conjugate pair of imaginary eigenfrequencies appear signalling a helical instability of the A_{C_2} phase. Figure 2 shows the evolution from the dispersion relation from the region of a stable A_{C_2} phase indicated by positive frequencies. Negative values correspond to the magnitude of the imaginary frequencies of the unstable NG mode. The wavevector of the most unstable mode, $Q_c(T)$, is indicated at each temperature. As we show below the instability is stabilized to a new chiral phase with spontaneously broken translation symmetry along z by nonlinear terms in the GL free energy.

Double Helix Phase — The structure of the broken translation symmetry of this new phase, designated as S_A , is that of a *double helix*, easily visualized by the propagating rotation of the pair dislocations as shown in Fig. 1. This phase has continuous *helical* symmetry under the set of rotations by $-\Theta$ about \hat{z} , $R_z[-\Theta]$ combined with the translation along z a distance $+\Theta/Q$, $T_z[+\Theta/Q]$. Note also the helical flow of the counter-propagating supercurrents that are confined near the two dislocations. The model for the order parameter in Eq. 9 allows us to study the temperature evolution of the equilibrium S_A phase, with rotary propagation $\vartheta(z) = Qz$, shown in Fig. 3. Note that half-period, $L = \pi/Q$, is a minimum at the S_A - P_z transition, with $L \approx 37 \xi_0 \approx 674$ nm at $p = 26$ bar, and diverges as the S_A - A_{C_2} transition is approached. The structure of the S_A phase obtained from the variational model, as well as the second-order phase transitions between A_{C_2} - S_A phases, and S_A - P_z phase, agree closely with the numerical minimization of the full GL functional (see Appendix).

Phase Diagram — We find six distinct phases for cylindrical channels: the translationally invariant P_z , $A_{SO(2)}$, A_{C_2} , and $B_{SO(2)}$ phases reported in Ref. [8], the double helix S_A phase, and a periodic domain-wall B-phase, S_B , predicted by Aoyama [21]. The S_B phase is defined by domain walls separating polar-distorted B-like phases along the z axis. We impose boundary conditions for the half-period, L , of the order parameter at $z = 0$ and $z = L$,

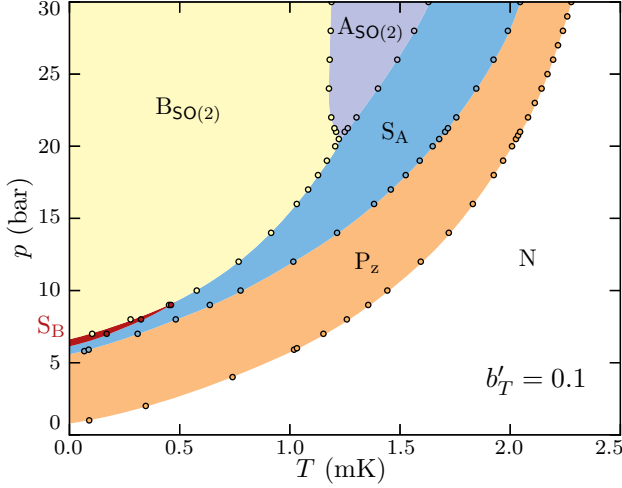


FIG. 4. Phase diagram for the cylindrical channel with $R = 100\text{nm}$ and strong pairbreaking, $b'_T = 0.1$. The labels S_A and S_B correspond to the helical and B-like stripe phases, respectively. The $A_{SO(2)}$ phase appears at the highest pressures, and the AC_2 phase is suppressed by the more stable S_A phase. The S_B phase appears in a narrow region at low pressure and low temperature.

where L is determined in the minimization of the free energy functional.

Figure 4 shows the phase diagram for a $R = 100\text{nm}$ cylindrical channel with strong pairbreaking, $b'_T = 0.1$. The polar P_z phase, with Cooper pairs nematically oriented along the channel is the first superfluid phase to nucleate from the normal state. At a lower temperature the transverse orbital components appear; the chiral S_A phase develops at second-order instability from the P_z phase. Compared to an earlier calculation [8] that assumed translational invariance along the channel, we find that the AC_2 phase is replaced by the more stable S_A phase. At the higher pressures, the isotropic chiral A phase is favored over the helical phase, separated by a first-order transition line, which then terminates at a tricritical point, below which the helical phase is unstable to the polar-distorted B phase, $B_{SO(2)}$, also separated by a first-order transition. At still lower pressures the S_B phase is stable in a very small window of the phase diagram. The $A_{SO(2)}$ and S_B phases are very sensitive to surface pair-breaking, and are completely suppressed for maximal pairbreaking (see Appendix). Finally, as the surface boundary condition approaches specular reflection the AC_2 and S_A phases are supplanted by the $A_{SO(2)}$ phase. A more detailed presentation of the phase diagram, including a phase diagram as a function of channel radius R , is presented in the Appendix.

NMR Signatures — Nuclear magnetic resonance (NMR) spectroscopy is a tool for identifying inhomogeneous phases of superfluid ^3He [22]. The frequency shift of the NMR line relative to the Larmor frequency is sensitive to the spin and orbital correlations of the order parameter that minimizes the nuclear magnetic dipole energy, $\Delta\Omega_D = \int_V d^3r g_D (|\text{Tr}A|^2 + \text{Tr}AA^*)$. The dipole energy lifts the degeneracy of the equilibrium states with respect to rela-

tive spin-orbit rotations. Thus, deviations from the minimum dipole energy configuration lead dipolar torques generated by the spin-triplet Cooper pairs that shift the NMR resonance frequency away from the Larmor frequency. The magnitude of the shift is determined by the dipole coupling, $g_D = \frac{\chi_N}{2\gamma^2} \Omega_A^2 / \Delta_A^2$, which can be expressed in terms of normal-state spin susceptibility, χ_N , and the bulk A-phase longitudinal resonance frequency, Ω_A . We follow the analysis described in Ref. [8] for the transverse NMR frequency shifts of the translationally invariant phases of ^3He confined in nano-pores to calculate the frequency shifts of the S_A phase. In particular, the spatially averaged dipole energy density for the S_A phase is $f_D = g_D \langle \Delta^2 \rangle_{S_A} (\hat{d} \cdot \hat{z})^2$, with $\langle \Delta^2 \rangle_{S_A} = 2 \langle \Delta_z^2 \rangle - \langle \Delta_\phi^2 \rangle - \langle \Delta_r^2 \rangle$ where $\langle \Delta_i^2 \rangle = \int_V d^3r \sum_\alpha |A_{\alpha i}|^2$ and \hat{d} lies in the plane of the channel and perpendicular to the static magnetic field axis \hat{H} . This results in a frequency shift of the same form as that of the P_z and $A_{SO(2)}$ phases [8], but with amplitude $\propto \langle \Delta^2 \rangle_{S_A}$,

$$\omega\Delta\omega = \frac{\gamma^2}{\chi_N} g_D \langle \Delta^2 \rangle_{S_A} \left[\cos\beta - \sin^2\theta \left(\frac{5\cos\beta - 1}{4} \right) \right], \quad (12)$$

where β is the pulsed NMR tipping angle and θ is the angle of the static field relative to the z axis. Figure 5 shows the frequency shift for $\beta \rightarrow 0$ as a function of temperature for the S_A variational order parameter defined in Eq. 9 and plotted in Fig. 3 for two field orientations. The second order transition at the P_z - S_A boundary shows a discontinuity in the slope of $\Delta\omega(T)$, and an apparent jump occurs at the S_A - AC_2 transition. In fact this is a smooth crossover confined to a narrow temperature range related to the divergence of the period of the S_A phase. The detailed NMR spectrum close to this transition is more complex because the spatial variations of the S_A phase, set by the half-period, L , can exceed the dipole coherence length, $\xi_D \equiv \sqrt{g_D/K_1} \approx 10\mu\text{m}$ near to the S_A - AC_2 transition. The \hat{d} vector becomes inhomogeneous, spatial averaging breaks down and the NMR line will broaden as the temperature approaches the S_A - AC_2 transition in a narrow window indicated by the gray shading in Fig. 5. A narrow NMR line is restored in the AC_2 phase.

Conclusions and Beyond ^3He — We find six distinct equilibrium phases within highly confined cylindrical channels, including two phases that break translation symmetry along the channel. In particular, we predict a “helical” phase, S_A , which spontaneously breaks time-reversal symmetry and translational symmetry, but retains rotary-translation (helical) symmetry. The double-helix structure of this phase is predicted to be stable over a significant region of p-T phase diagram for long cylindrical pores of radius approaching the Cooper pair coherence length ξ_0 , and to show a distinct NMR signature.

The novel broken symmetry phases of ^3He are based on competing interactions in a strongly correlated Fermi liquid with unconventional pairing, combined with strong pair breaking by confining boundaries. This situation can arise in a broad range of unconventional superconductors, including chiral superconductors such as Sr_2RuO_4

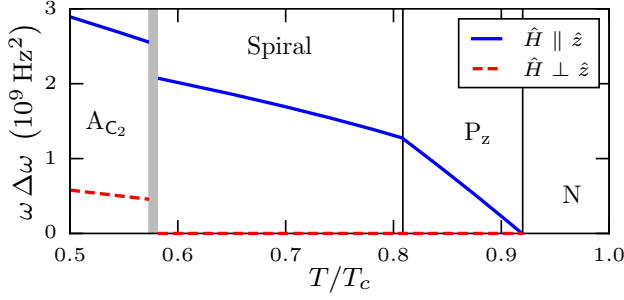


FIG. 5. Small tipping angle ($\beta \approx 0$) transverse frequency shift for the S_A phase as a function of temperature. The S_A phase order parameter is that shown in Fig. 3. The S_A and P_z frequency shifts are found using Eq. 12, and the A_{C_2} frequency shifts are given by Eqs. 36 and 37 in Ref. 8. The grey shaded region denotes the region of the S_A phase where the half-period L exceeds $\xi_D \approx 10 \mu\text{m}$.

and UPT_3 , as well as the cuprates. Indeed theoretical predictions of novel broken translational symmetry phases are reported for d-wave superconductors subject to strong confinement [23, 24], and it seems likely that there are more novel broken symmetry phases in multi-component, unconventional superconductors awaiting discovery.

Acknowledgements — This research was supported by National Science Foundation Grant DMR-1508730. We thank Bill Halperin and Andrew Zimmerman for discussions on confined phases of ^3He that contributed to this research. We also thank Michael Moore for bringing Ref. 6 to our attention.

APPENDIX

Order Parameter for the Double Helix Phase — Numerical minimization of the GL functional to determine the exact structure of the S_A phase is made efficient, without loss of accuracy, by developing the ϕ -dependence as an expansion in symmetry-preserving harmonics,

$$A_{\alpha i} = \hat{d}_\alpha \sum_{j=0}^{\infty} \left\{ \begin{aligned} &\Delta'_{r,j}(r) \sin[2j(\phi + Qz)] \hat{r}_i \\ &+ i \Delta''_{r,j}(r) \cos[(2j+1)(\phi + Qz)] \hat{r}_i \\ &+ \Delta'_{\phi,j}(r) \cos[2j(\phi + Qz)] \hat{\phi}_i \\ &+ i \Delta''_{\phi,j}(r) \sin[(2j+1)(\phi + Qz)] \hat{\phi}_i \\ &+ \Delta'_{z,j}(r) \cos[2j(\phi + Qz)] \hat{z}_i \\ &+ i \Delta''_{z,j}(r) \sin[(2j+1)(\phi + Qz)] \hat{z}_i \end{aligned} \right\}. \quad (13)$$

The numerical result for the S_A phase converges rapidly to the exact solution with the addition of higher harmonics.

Sensitivity of the Phase Diagram to Strong Pairbreaking — The anisotropic chiral A_{C_2} and S_A phases are favored under conditions of strong pairbreaking on the boundary because the energy cost of the boundary half-disgyrations is minimal due to suppression of all the order parameter components. By contrast the $A_{SO(2)}$ phase, which hosts a

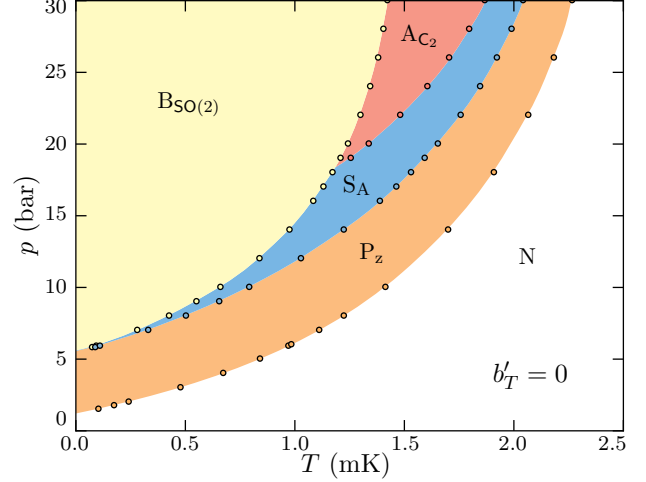


FIG. 6. Phase diagram for the cylindrical channel with $R = 100\text{nm}$ and $b'_T = 0$ (maximal pairbreaking). The S_A phase has displaced much of the A_{C_2} phase compared to the phase diagram calculated for only z translationally invariant phases [8].

radial disgyration at the center of the cell is disfavored over both anisotropic chiral phases.

This is reflected in the phase diagram for maximal pair-breaking, $b'_T = 0$, shown in Fig. 6 for a $R = 100\text{nm}$ cylindrical channel. Note that strong-coupling, which is relatively stronger at higher temperatures favors the helical phase over the translationally invariant A_{C_2} phase. Also note that S_B phase is not stable at this confinement ($R = 100\text{nm}$) for maximal pair-breaking.

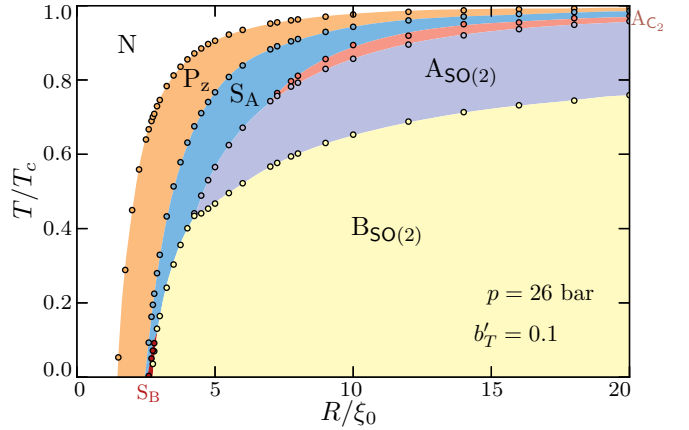


FIG. 7. Phase diagram: temperature versus radius for cylindrical channel at $p = 26\text{bar}$ with strong pairbreaking. $b'_T = 0.1$. All six phases we have found are shown in this diagram, although the S_B phase is stable in a very narrow window of R and T .

We also include the phase diagram as a function of the channel radius R (Fig. 7) for $p = 26\text{bar}$ and $b'_T = 0.1$. The S_A phase is clearly favored by high confinement relative to the A_{C_2} , $A_{SO(2)}$, and $B_{SO(2)}$ phases. However, at this pressure the S_B phase is very fragile and stable only at very low temperatures where non-local corrections to the gradient energy, which are not included in the extended GL

functional, are likely relevant. We also note that there is a critical radius above which the A_{C_2} phase appears.

* sauls@northwestern.edu

- [1] G. E. Volovik and M. A. Zubkov, *Nambu sum rule and the relation between the masses of composite Higgs bosons*, Phys. Rev. D **87**, 075016 (2013).
- [2] J. A. Sauls and T. Mizushima, *On the Nambu Fermion-Boson Relations for Superfluid ^3He* , Phys. Rev. B **95**, 094515 (2017).
- [3] A. J. Leggett, *Theoretical Description of the New Phases of Liquid ^3He* , Rev. Mod. Phys. **47**, 331 (1975).
- [4] G. E. Volovik, *The Universe in a Helium Droplet* (Clarendon Press, Clarendon, UK, 2003).
- [5] T. Mizushima, Y. Tsutsumi, T. Kawakami, M. Sato, M. Ichioka, and K. Machida, *Symmetry Protected Topological Superfluids and Superconductors - From the Basics to ^3He* , J. Phys. Soc. Jpn. **85**, 022001 (2016).
- [6] G. Barton and M. A. Moore, *Superfluid ^3He in restricted geometries*, J. Low Temp. Phys. **21**, 489 (1975).
- [7] A. B. Vorontsov and J. A. Sauls, *Crystalline Order in Superfluid ^3He Films*, Phys. Rev. Lett. **98**, 045301 (2007).
- [8] J. J. Wiman and J. A. Sauls, *Superfluid phases of ^3He in nanoscale channels*, Phys. Rev. B **92**, 144515 (2015).
- [9] J. J. Wiman and J. A. Sauls, *Strong-Coupling and the Stripe Phase of ^3He* , J. Low Temp. Phys. **184**, 1054 (2016).
- [10] E. Thuneberg, *Ginzburg-Landau theory of vortices in superfluid $^3\text{He-B}$* , Phys. Rev. B **36**, 3583 (1987).
- [11] A. Abrikosov, *On the Magnetic Properties of Superconductors of the Second Group*, Sov. Phys. JETP **5**, 1174 (1957).
- [12] D. F. Agterberg and K. Yang, *The effect of impurities on Fulde-Ferrell-Larkin-Ovchinnikov superconductors*, J. Phys. Cond. Matt. **13**, 9259 (2001).
- [13] H. Choi, J. P. Davis, J. Pollanen, T. Haard, and W. Halperin, *Strong coupling corrections to the Ginzburg-Landau theory of superfluid ^3He* , Phys. Rev. B **75**, 174503 (2007).
- [14] D. Rainer and J. W. Serene, *Free Energy of Superfluid ^3He* , Phys. Rev. B **13**, 4745 (1976).
- [15] J. A. Sauls and J. W. Serene, *Potential Scattering Models for the Quasiparticle Interactions in Liquid ^3He* , Phys. Rev. B **24**, 183 (1981).
- [16] J. A. Sauls and J. W. Serene, *Higher-Order Strong Coupling Effects in Superfluid ^3He* , Physica B+C **108**, 1137 (1981).
- [17] J. W. Serene and D. Rainer, *The Quasiclassical Approach to ^3He* , Phys. Rep. **101**, 221 (1983).
- [18] V. Ambegaokar, P. de Gennes, and D. Rainer, *Landau-ginzburg equations for an anisotropic superfluid*, Phys. Rev. A **9**, 2676 (1974).
- [19] L. J. Buchholtz and A. L. Fetter, *Textures in superfluid $^3\text{He-A}$: Hydrodynamic and magnetic effects in a cylindrical pore*, Phys. Rev. B **15**, 5225 (1977).
- [20] T. Mizushima and J. A. Sauls, *Bosonic Surface States and Acoustic Spectroscopy of Confined Superfluid $^3\text{He-B}$* , arXiv **1801.02277**, 5 (2018).
- [21] K. Aoyama, *Stripe order in superfluid ^3He confined in narrow cylinders*, Phys. Rev. B **89**, 140502 (2014).
- [22] V. V. Dmitriev, D. A. Krasnikhin, N. Mulders, A. A. Senin, G. E. Volovik, and A. N. Yudin, *Orbital glass and spin glass states of $^3\text{He-A}$ in aerogel*, JETP Lett. **91**, 599 (2010).
- [23] A. B. Vorontsov, *Andreev bound states in superconducting films and confined superfluid ^3He* , Phil. Trans. Roy. Soc. A **376**, 20150144 (2018).
- [24] P. Holmval, A. B. Vorontsov, M. Fogelström, and T. Löfwander, *Broken translational symmetry at edges of high-temperature superconductors*, Nature Communications **9**, 2190 (2018).